



Contents lists available at ScienceDirect

Journal of Rock Mechanics and Geotechnical Engineering

journal homepage: www.jrmge.cn

Full Length Article

Modelling erosion of a single rock block using a coupled CFD-DEM approach

Penghua Teng^{a,*}, Fredrik Johansson^b, J. Gunnar I. Hellström^a^a Division of Fluid and Experimental Mechanics, Department of Engineering Sciences and Mathematics, Luleå University of Technology, Luleå, SE-971 87, Sweden^b Division of Soil and Rock Mechanics, KTH Royal Institute of Technology, Stockholm, SE-100 44, Sweden

ARTICLE INFO

Article history:

Received 11 August 2022

Received in revised form

1 April 2023

Accepted 15 June 2023

Available online 27 June 2023

Keywords:

Rock erosion

Block removal

Incipient motion

Coupled CFD-DEM

Critical shear stress

ABSTRACT

Rock block removal is the prevalent physical mechanism for rock erosion and could affect the stability of dam foundations and spillways. Despite this, understanding of block removal is still inadequate because of the complex interactions among block characteristics, hydraulic forces, and erosive processes acting on the block. Herein, based on a previously conducted physical experiment of erosion of a single rock block, the removal processes of two different protruding blocks are represented by a coupled computational fluid dynamics-discrete element model (CFD-DEM) approach under varied flow conditions. Additionally, the blocks could be rotated with respect to the flow direction to consider the effect of the discontinuity orientation on the block removal process. Simulation results visualize the entire block removal process. The simulations reproduce the effects of the discontinuity orientation on the critical flow velocity inducing block incipient motion and the trajectory of the block motion observed in the physical experiments. The numerical results present a similar tendency of the critical velocities at different discontinuity orientations but have slightly lower values. The trajectory of the block in the simulations fits well with the experimental measurements. The relationship between the dimensionless critical shear stress and discontinuity orientation observed from the simulations shows that the effect of block protrusion becomes more dominant on the block incipient motion with the increase of relative protrusion height. To our knowledge, this present study is the first attempt to use the coupled finite volume method (FVM)-DEM approach for modelling the interaction behavior between the block and the flowing water so that the block removal process can be reproduced and analyzed.

© 2023 Institute of Rock and Soil Mechanics, Chinese Academy of Sciences. Production and hosting by Elsevier B.V. This is an open access article under the CC BY license (<http://creativecommons.org/licenses/by/4.0/>).

1. Introduction

Rock erosion induced by fluid flow is a complex process in the evolution of natural landscapes. Rock erosion in bedrock channels can be problematic for important parts of power stations such as dam foundations, spillway channels, and other hydraulic structures (Annandale, 2006; Lamb et al., 2015). The progression of rock erosion downstream dams may compromise the stability of their foundations and spillways, and even shorten their life (Coleman et al., 2003; Billstein et al., 2006; George and Sitar, 2012; Pells et al., 2015). Consequently, the existence of erosion leads to high remediation costs and even poses a considerable risk to dam safety.

Accordingly, it is essential to predict and prevent rock erosion in these types of projects with unfavourable hydraulic conditions.

The rock erosion process in bedrock channels implies that hydraulic forces remove bedrock blocks (Wohl, 1993; Whipple et al., 2000a,b; Chatanantavet and Parker, 2009). The incipient motion of the rock block occurs when the erosive capacity of the flowing water exceeds the ability of the rock block to resist it (Annandale, 2006; George and Sitar, 2016). For developed turbulent flows, hydraulic erosional capacity mainly depends upon the dynamic water pressure, the stream power, or the shear stresses (Coleman et al., 2003; Billstein et al., 2006; Lamb et al., 2015; Dubinski and Wohl, 2013). The resistance of the rock blocks relies on their material parameters and the characteristics of the rock joints, such as the strength of the intact rock, the block weight and size, the block shape, the joints spacing and the joint orientations (Wohl, 1993; Annandale, 2006; Chatanantavet and Parker, 2009; Li and Liu, 2010). The complex interactions between flowing water and

* Corresponding author.

E-mail address: penghua.teng@ltu.se (P. Teng).

Peer review under responsibility of Institute of Rock and Soil Mechanics, Chinese Academy of Sciences.

bedrock dominate the process of rock erosion, resulting in a challenge in predicting the occurrence of rock erosion.

Extensive investigations have studied the incipient motion of rock blocks subjected to a variety of flow conditions, including open channels, hydraulic jumps and plunge pools (Fiorotto and Rinaldo, 1992; Bollaert, 2002; Coleman et al., 2003; Bollaert and Schleiss, 2005; Annandale, 2006; Chatanantavet and Parker, 2009; Duarte, 2014). Semi-empirical and physically based approaches, such as the erodibility index method (EIM) (Annandale, 1995, 2006) and the comprehensive scour model (CSM) (Bollaert, 2002), are typically used to predict the threshold condition of the motion of the rock blocks, since they are simplified and can be widely applied to various flow conditions. The approaches commonly determine the incipient rock block motion by comparing the erosive capacity of the flowing water against the erodibility of the rock mass (George, 2015; George and Sitar, 2016). These models seldom reflect the actual mechanism of the rock erosion process. Insights into the mechanism are, therefore, essential to improve the understanding of the rock erosion process. Scaled hydraulic model tests have been conducted to represent the rock erosion failure modes such as block removal, brittle failure and fatigue failure (Coleman et al., 2003; Melville et al., 2006; Chatanantavet and Parker, 2009; Dubinski and Wohl, 2013; Lamb et al., 2015). Despite these efforts, experimental studies rarely managed to represent the erosion process that appeared in field sites. To simplify the complex problem that erosion constitutes in the field, a local rock erosion process is usually studied experimentally in a laboratory, e.g. erosion of a single rock block (Bollaert, 2002; Coleman et al., 2003; Melo et al., 2006; Federspiel et al., 2009; Asadollahi et al., 2011; George, 2015). Koulibaly et al. (2022) conducted a laboratory-scale physical model to determine the effects of rock mass parameters on erosion. They studied individual and interactive effects of several hydraulic and rock mass parameters on erosion. In nature, however, the occurrence of rock erosion involves more complex three-dimensional (3D) rock geometries comprised of multiple blocks and various flow conditions. Hence, a reliable method to handle real-life scenarios is needed.

To complement semi-empirical approaches and physical model tests, numerical methods are an alternative means to model the rock erosion process, even under the prototype scale. A computational fluid dynamics (CFD) model has been combined with a two-dimensional (2D) universal distinct element code by Dasgupta et al. (2011), and curvilinear immersed boundary method was used by Khosronejad et al. (2011, 2013) to estimate the erosion formation induced by flowing water. These numerical models first represent the flowing water features from the CFD simulations; and thereafter, the obtained flow features are used as input parameters by the other solver that evaluates the occurrence of the erosion of the rock/channel bed. Although these numerical methods cannot fully describe the interaction behavior between flowing water and the surface of the bedrock, they still help to improve the understanding of the erosion process.

In the past decades, particle-fluid flows have been successfully simulated by different numerical approaches, in which the coupled lattice Boltzmann method (LBM)-discrete element model (DEM) and CFD-DEM approaches have been mostly used in engineering applications, e.g. hydraulic fracturing, coastal sediment transport, gas-solid fluidization, and aerosol deposition. Besides, Robinson et al. (2014) employed a coupled smoothed particle hydrodynamics (SPH)-DEM to simulate single and multiple particle sedimentation in a 3D fluid column.

The LBM coupling with the DEM has been developed in recent decades (Han and Cundall, 2011; Owen et al., 2011; Galindo-Torres, 2013; Zhang et al., 2014; Soundararajan, 2015; Rettinger and Rüde, 2022). LBM is a class of CFD methods, which discretizes the fluid

domain at the mesoscopic scale where the discrete Boltzmann equation is solved with a collision model. The primary variable is the distribution function. The macroscopic variables, e.g. density and velocity, are calculated indirectly. Wang (2019) investigated the proppant transport and the conductivity of proppant-packed hydraulic fractures by using the LBM-DEM approach. It is worth noticing that Gardner and Sitar (2019) employed a coupled LBM-DEM approach to evaluate the potential for rock erosion induced by fast flowing water in rock channels, which simulates the dynamic interactions between the rock block and its surrounding flow.

In this paper, an unresolved coupled CFD-DEM approach is employed to simulate rock erosion processes. In the approach, the Navier-Stokes equations are solved by the finite volume method (FVM) to describe the fluid motion and the movement of individual particles is simulated by DEM following the Newton's law. The approach has been successfully used in particle-laden flows such as sediment transportation, geodynamical magmatic and seepage flows (Chen et al., 2011; Furuichi and Nishiura, 2014; Zhao et al., 2014; Fantin, 2018; Teng et al., 2021). Previous studies have shown that the approach could reasonably capture not only the motion of spherical particles under various flow conditions (Zhou et al., 2010; Schmeeckle, 2014; Sun and Xiao, 2016a,b), but also handle behaviors of non-spherical rigid bodies derived by flowing water (Krugger-Emden et al., 2008; Guo et al., 2012; Sun et al., 2017). Accordingly, the coupled CFD-DEM approach has a great potential to be a suitable tool for simulating the erosion process of rock blocks; in this paper, the approach is used for the first time in an attempt to model the rock erosion process. Since the erosion of rock blocks highly depends on the interaction between the flowing water and the rock blocks, the approach is expected to capture the responses of a rock block when impacted by external flows.

This study adopts the coupled CFD-DEM approach to reproduce the rock erosion processes observed in the experimental tests by George (2015) at the University of California's Richmond Field Station. He conducted scaled hydraulic model tests in order to investigate the influence of discontinuity orientation on block erodibility over a range of flow scenarios. The experimental results not only determined the threshold of the incipient motion of rock blocks, but also reflected the failure mode of rock block erosion, i.e. block removal. Based on the rock block geometries in the experiments, this study reproduces two 3D rock blocks. After that, the coupled CFD-DEM approach is used to represent the blocks' removal process under various flow scenarios. The simulation results are used to determine the threshold of the rock blocks' incipient motion and then examine their subsequent motion trajectories. Finally, a comparison with experimental data from George (2015) is performed, and the results are discussed.

2. Methodology

2.1. Coupled CFD-DEM framework

The coupled CFD-DEM approach consists of two open-source software packages: OpenFOAM and LIGGGHTS. In the numerical framework, the fluid behaviors described by Navier-Stokes equations are solved with the aid of CFD, whereas the dynamics of a particle are described using Newton's law and simulated by DEM. The DEM assumes that the material, i.e. granular matter, bulk material and rocks, is made of separate, discrete particles. Thanks to a CFD-DEM engine, it facilitates accomplishing the coupling process between fluids and particles. The coupling process is presented in Section 2.1.3. Details of the two software package codes can be found in Kloss et al. (2012) and Goniva et al. (2012).

2.1.1. Fluid motion model

In this study, fluid motions are modeled by a large eddy simulation (LES), wherein the spatially-filtered 3D Navier-Stokes equations are directly solved over time. As such, the eddy motions with a scale larger than the mesh size of the numerical grid are resolved, while smaller-scale motions are modeled using a sub-grid scale model.

The fluid momentum equation is formulated as

$$\rho_f \left(\frac{\partial \varepsilon_f \mathbf{v}_f}{\partial t} + \nabla \cdot (\varepsilon_f \mathbf{v}_f \mathbf{v}_f) \right) = -\nabla p - \mathbf{f}_f^p + \nabla \cdot \boldsymbol{\tau} + \rho_f \varepsilon_f \mathbf{g} \quad (1)$$

where ρ_f is the density of fluid (kg/m^3); \mathbf{v}_f is the velocity of fluid (m/s); \mathbf{g} is the acceleration of gravity (m/s^2); ε_f is the volume fraction occupied by the fluid in a cell; ∇p is the pressure gradient; $\mathbf{f}_f^p = \sum_{i=1}^{N_p} \mathbf{f}_{pi}^f / \Delta V$ is the force per unit volume of the particles acting on the fluid, in which ΔV is the mesh-cell volume (m^3); N_p is the particle number inside the cell; and \mathbf{f}_{pi}^f is the interaction force imposed by the fluid to the i th particle in the cell. $\boldsymbol{\tau} = -2\nu_t \bar{S}_{ij}$ is the unresolved subgrid stress provided by the dynamic Smagorinsky model (Germano et al., 1991), where \bar{S}_{ij} is the resolved rate of strain and $\nu_t = (C_s \Delta)^2 \sqrt{2\bar{S}_{ij}\bar{S}_{ij}}$ is the sub-grid scale eddy viscosity in which Δ is the characteristic filter length, i.e. the cubic root of the cell volume and C_s is the Smagorinsky constant dynamically computed to adapt to local flow conditions. The LES model has been widely used for modeling flow around bluff bodies (Lysenko et al., 2012, 2014; Lloyd and James, 2015; Etminan et al., 2017).

Herein, all simulations are performed in a domain of $2.193 \text{ m} \times 0.3 \text{ m} \times 0.864 \text{ m}$ in the streamwise (x), vertical (y) and cross-stream (z) directions, respectively, as shown in Fig. 1, and L is the length of the block mold. The direction of the acceleration of gravity is 77.5° from the bottom of the domain to mimic the flow conditions in George (2015)'s experiments. The geometry of the block mold is simplified based on the tetrahedral mold used in the experiments by George (2015). The block tip at the bottom of the mold is truncated to facilitate the structured grid generation in the block mold region in order to improve the numerical stability of the simulations. The dimension of the modified block mold is illustrated in Table 1. The origin of the coordinate is at the middle point of edge 1. The block mold is $5L$ away from the inlet of the computational domain and at a distance of $10L$ from the outlet. The inlet and outlet surfaces are selected as the water velocity inlet and pressure outlet (atmospheric pressure) boundary conditions, respectively. The top of the domain is treated as a frictionless rigid lid, and a no-slip wall boundary condition is applied at the bottom of the domain and at the side surfaces.

Fig. 2a shows the grid of the domain. The computational grid contains 522,000 cells. The mesh is refined around the block mold to better capture the interaction between the flowing water and the rock block. The first cell distance of the surfaces of the bottom and

Table 1

Dimensions of block mold.

Edge	Dimension (m)
1	0.11
2	0.1477
3	0.1477
4	0.0881
5	0.0881
6	0.1
7	0.0219
8	0.0293
9	0.0293

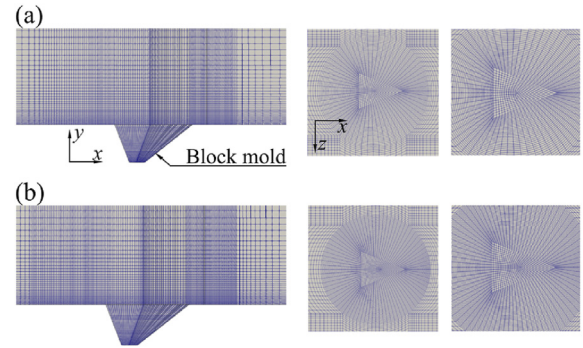


Fig. 2. Grid of computational domain: (a) Normal grid, and (b) Finer grid.

block mold is 2.4 mm . Since unresolved coupling CFD-DEM used in this study deals with particles' size (introduced in the following section) smaller than the CFD computational grid, the smallest size of the grid cell, $2.8 \text{ mm} \times 2.4 \text{ mm} \times 2.8 \text{ mm}$, is close to the particle size to increase the accuracy of the fluid-filled void area. In addition, to study the grid independence of the simulation, a more refined grid shown in Fig. 2b is also generated. The number of cells is 722,000, with the increased mesh resolution around the block mold.

2.1.2. Particle motion model

The DEM is a Lagrangian method used for calculating the dynamics of each particle. The force and torque equations are based on Newton's second law and are written as follows:

$$m_p \frac{d\mathbf{v}_p}{dt} = \mathbf{f}_p^g + \mathbf{f}_p^c + \mathbf{f}_p^f \quad (2)$$

$$I_p \frac{d\boldsymbol{\omega}_p}{dt} = \mathbf{T}_p^c + \mathbf{T}_p^f \quad (3)$$

where \mathbf{v}_p and $\boldsymbol{\omega}_p$ are the translational (m/s) and angular velocities (rad/s) of an individual particle, respectively; $\mathbf{f}_p^g = m_p \mathbf{g}$ is the gravitational force (N), in which m_p is the mass of a particle (kg); \mathbf{f}_p^c is the contact force (N) due to interparticle collisions; and \mathbf{f}_p^f is the particle-fluid interaction force (N) acting on each particle by surrounding fluid (introduced in Section 2.1.3); I_p is the angular moment of inertia (kg m^2); \mathbf{T}_p^c is the torques ($\text{kg m}^2/\text{s}^2$) arising from particle-particle or particle-wall collisions, which is computed by inter-particle contact represented by an elastic spring and a viscous damper. Further details are available in the work of Tsuji et al. (1993). \mathbf{T}_p^f is the torques ($\text{kg m}^2/\text{s}^2$) due to the particle-fluid interaction forces acting on the centroid of a particle.

2.1.2.1. (1) generation of irregular rock blocks. Two tetrahedral rock blocks were used in George (2015)'s experiments to investigate the

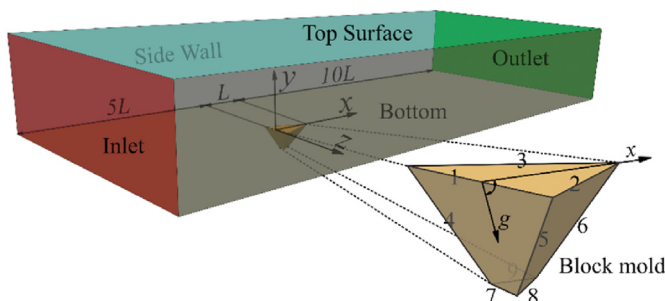


Fig. 1. Computational domain of simulations.

effect of rock protrusion height on the erosion process. In this study, based on the block geometries used in the experiments (George, 2015), two simplified rock blocks shown in Fig. 3 are generated by the multi-sphere method (Kruggel-Emden et al., 2008; Amberger et al., 2012). The method clumps multiple particles together and integrates them as one rigid body and then employs a Monte Carlo resampling procedure to calculate the clump volume, mass and center of mass (Amberger et al., 2012; Nan et al., 2022; Shen et al., 2022). Fig. 3b shows the reproduced blocks A and B. They consist of 2820 and 3120 spherical particles with a constant diameter of 0.002 m, respectively, in which the degree of overlap between the particles is 12%. The approximations of the geometries for these two multi-spherical blocks are more than 90% compared to the dimensions of the blocks used by George (2015). The dimensions of the blocks are listed in Table 2.

2.1.2.2. (2) contact force. Thanks to the multi-sphere method, the algorithm of the contact force detection for multispheres is the same as the method used for single spherical particles. Total forces and torques on each multisphere are thus computed as the sum of the forces and torques on its constituent particles. The contact force model is formulated by springs in both tangential and normal directions based on the work by Mindlin and Deresiewicz (1952), which employs the Hertzian contact theory and the tangential force displacement relationship. This study treats the multisphere as an elastic body, whereas the boundary is defined as a stiffness wall. The \mathbf{f}_p^c due to particle-particle or particle-wall collisions consisting of normal \mathbf{f}_n and tangential \mathbf{f}_s forces (N) is written as follows:

$$\mathbf{f}_p^c = \mathbf{f}_n + \mathbf{f}_s = (k_n \delta_n - r_n \mathbf{v}_n) + (k_t \delta_t - r_t \mathbf{v}_t) \tag{4}$$

where \mathbf{v}_n and \mathbf{v}_t are the relative velocities (m/s) of the two particles in normal and tangential directions, respectively; and δ_n and δ_t are the overlap distance (m) of two particles in the normal and tangential direction, respectively. The elastic stiffnesses of a particle (N/m) in the normal and tangential directions are

$$k_n = \frac{4}{3} E^* \sqrt{R^* \delta_n} \tag{5}$$

$$k_t = 8 G^* \sqrt{R^* \delta_n} \tag{6}$$

where

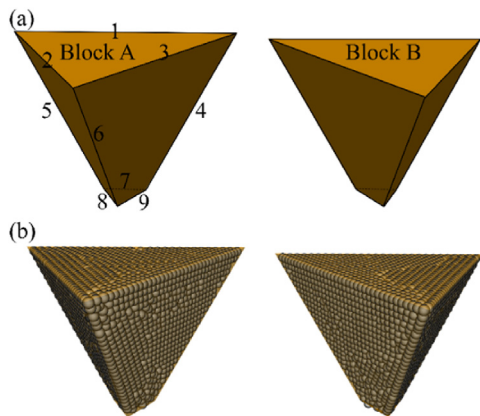


Fig. 3. Two blocks used in the simulations: (a) Geometries of the two blocks, and (b) Blocks reproduced by the multi-sphere method.

Table 2
Dimensions of the two blocks.

Edge	Block A dimension (m)	Block B dimension (m)
1	0.1066	0.1037
2	0.1402	0.1387
3	0.1402	0.1387
4	0.087	0.084
5	0.087	0.084
6	0.1083	0.1062
7	0.0189	0.0183
8	0.0248	0.0244
9	0.0248	0.0244

$$R^* = \frac{1}{R_i} + \frac{1}{R_j}, E^* = \frac{-\vartheta_i^2 + 1}{E_i} + \frac{-\vartheta_j^2 + 1}{E_j}, G^* = \frac{2(2 + \vartheta_i)}{E_i} + \frac{2(2 + \vartheta_j)}{E_j}$$

where R , E and ϑ are the radius, the Young's modulus and the Poisson's ratios of two contacting particles i and j . The viscoelastic damping constants (kg/s) of normal and tangential contact are

$$r_n = -2\sqrt{5/6}\beta\sqrt{s_n m^*} \tag{7}$$

$$r_t = -2\sqrt{5/6}\beta\sqrt{s_t m^*} \tag{8}$$

where $S_n = 2E^* \sqrt{R^* \delta_n}$, $S_t = 8G^* \sqrt{R^* \delta_n}$, $m^* = \frac{1}{m_{pi}} + \frac{1}{m_{pj}}$ and $\beta = \frac{\ln e}{\sqrt{(\ln e)^2 + \pi^2}}$, in which e is the coefficient of restitution.

All parameters of the contact model are presented in Table 3. The density of the blocks is set as the values measured in the experiments. Since previous numerical studies have demonstrated a negligible effect of the decreased value of Young's modulus (E) on the particles' physical behaviors in the DEM model (Zhou et al., 2010; Chand et al., 2012; Zhao and Shan, 2013), a magnitude of 5×10^8 Pa less than real values is chosen for E to decrease the time-step size of the simulations. George (2015) conducted block yield tests where the block mold was inclined from near horizontal to sub-vertical until the block slide out. From the tests, the angle of wall friction was determined to 16° . Accordingly, the coefficient of friction for the particle-wall contact in the DEM model is set to 0.286. The value of the coefficient of restitution is 0.01, since the rebound induced by particle collisions is assumed to be negligible.

2.1.3. CFD-DEM coupling process

The coupling process between CFD and DEM is accomplished through the particle-fluid interaction force model, which is detailed in the work of Zhou et al. (2010). The forces acting on the particle are calculated based on the volume fraction of particles and mean particle velocity in a CFD cell when the particles in the CFD cell are located. The formulation of the interaction force, \mathbf{f}_p^f , is commonly problem-specific. This study aims to numerically represent the threshold of rock blocks' incipient motion and their subsequent

Table 3
Particle parameters.

Parameter	Unit	Value
Particle diameter	m	0.002
Coefficient of restitution		0.01
Poisson's ratio		0.45
Young's modulus	Pa	5×10^8
Coefficient of friction		0.286
Particle density	kg/m ³	2360

movement. Accordingly, the \mathbf{f}_p^f consists of the fluid pressure gradient, buoyancy, viscous, drag and lift forces since these forces mainly contribute to the interaction between a particle and the fluid (Zhou et al., 2010; Kloss et al., 2012). The \mathbf{f}_p^f is then formulated as

$$\mathbf{f}_p^f = \mathbf{f}_d + \mathbf{f}_l + \mathbf{f}_{\nabla p} + \mathbf{f}_v \quad (9)$$

where \mathbf{f}_d , \mathbf{f}_l , $\mathbf{f}_{\nabla p}$ and \mathbf{f}_v are the drag, lift, pressure gradient including the effect of buoyancy and viscous forces, respectively.

The \mathbf{f}_d is expressed by the following equation used in the work of Schmeeckle (2014), who modeled the sediment transport process from bedload to suspend-load condition:

$$\mathbf{f}_d = \frac{1}{8} \pi \rho_f C_d D^2 |\mathbf{v}_p - \mathbf{v}_f| (\mathbf{v}_p - \mathbf{v}_f) \quad (10)$$

where \mathbf{v}_p is the particle velocity vector (m/s) and C_d is the drag coefficient calculated as

$$C_d = \left(0.9 + \frac{4.8}{\sqrt{Re_r}} \right)^2 \quad (11)$$

where Re_r is the relative Reynolds number

$$Re_r = \frac{|\mathbf{v}_p - \mathbf{v}_f| \rho_f D}{\mu_f} \quad (12)$$

where μ_f is the dynamic water viscosity (kg/(m s)).

The \mathbf{f}_l acting on a spherical particle is modeled according to Saffman lift arising from the pressure distribution on a particle in a velocity gradient (Saffman, 1968) as

$$\mathbf{f}_l = C_l \rho_f \nu^{0.5} D^2 (\mathbf{v}_p - \mathbf{v}_f) \times |\mathbf{v}_p - \mathbf{v}_f| \quad (13)$$

where ν is the kinematic viscosity (m^2/s) and $C_l = 1.6$ is the lift coefficient.

The viscous and pressure gradient forces are defined as $\mathbf{f}_v = -\nu_p \times \nabla \cdot \boldsymbol{\tau}$ and $\mathbf{f}_{\nabla p} = -\nu_p \times \nabla p$, respectively.

2.2. Simulation cases

Fig. 4a shows the initial scenarios (simulation time, $t = 0$ s) of the blocks with different protrusion heights (h) between the block top surface and channel bed. The joint apertures for the two blocks are 2 mm corresponding to the value of fixed discontinuity opening

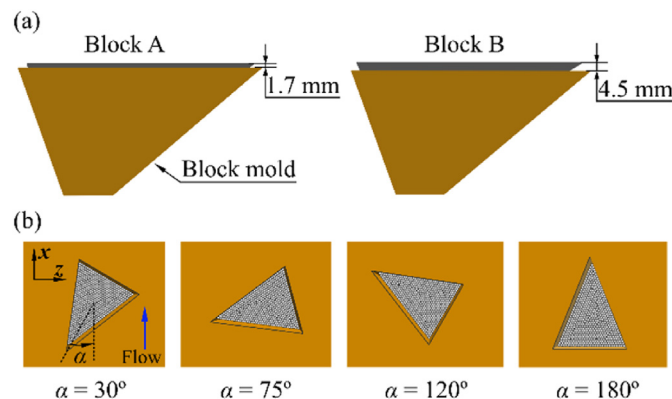


Fig. 4. Initial scenarios of blocks: (a) Protrusion heights (h) of the two blocks, and (b) Four different block model orientations.

used in the experiment conducted by George (2015). The block mold is varied at 30° , 75° , 120° and 180° (α) to change the block's orientation with respect to the streamwise direction (x positive direction) shown in Fig. 4b. Since George (2015) conducted a scaled physical model test, the flow velocities in the experiments are in a range of 2–3 m/s, which correspond to flow velocities of 6–10 m/s in the prototype level. For each simulation, a varied water velocity (\mathbf{u}_w) is imposed on the inlet surface shown in Fig. 1, and the value of \mathbf{u}_w is increased every 8 s with increments of 0.05 from 1 m/s to 3 m/s to determine the critical condition of incipient motion of the rock blocks. All simulation cases are listed in Table 4. A total of nine simulations are performed, in which case No. 5 with a finer grid is used to study the grid independence.

3. Results

3.1. Threshold of incipient motion

As described in Section 2.2, the value of \mathbf{u}_w in each simulation is gradually increased to ensure the occurrence of block motion in the simulation. Through the simulation results, the behaviors of the rock block can be clearly observed. In addition, to determine the threshold conditions of rock block motion, the streamwise displacement of the block, $S = x_c - x_{int}$, is monitored, in which x_c is the location of the centroid of the block in the x direction and x_{int} is the initial position of the centroid of the block in the x direction.

Fig. 5a–h presents the change of S with increasing \mathbf{u}_w . The value of S at each simulation's initial condition ($t = 0$) is 0 m. As the flowing water impacts the block, the block starts to move and reaches a temporary steady state, as shown in Fig. 5. After that, the block remains in a static state until \mathbf{u}_w increases to a critical value inducing the incipient motion of the block. The block subsequently starts to move and is finally taken out of the mold.

A combination of S values with the observed block positions is then used to determine the critical flow velocity, \mathbf{u}_{wc} , inducing the block incipient motion. Table 5 lists the value of \mathbf{u}_{wc} of each simulation case. For a fixed h value, the threshold condition for incipient motion of the blocks is highly dependent on the value of α . The block at $\alpha = 120^\circ$ presents a maximum resistance to scouring and a minimum at $\alpha = 75^\circ$. Based on previous works (Whipple et al., 2000b; Coleman et al., 2003; Dubinski and Wohl, 2013), it has been shown that increased block side length parallel to the flow increases the block stability, whereas increased side length perpendicular to the flow decreases the block stability. At $\alpha = 75^\circ$, the block has its maximum side length perpendicular to the flow and its minimum side length parallel to the flow. However, this suggestion is opposed to the block at $\alpha = 120^\circ$. The block profile protruding into the flow at $\alpha = 120^\circ$ is narrow, leading to a minimal drag force imposed on the block. In addition, the force induced on the block mold surfaces could also affect the erodibility of the block. For a fixed α value, the block is more erodible with a larger value of

Table 4
Simulation cases.

Case No.	u_w (m/s)	h (mm)	α ($^\circ$)
1	1–3	1.7	30
2			75
3			120
4			180
5			180 (refined grid)
6		4.5	30
7			75
8			120
9			180

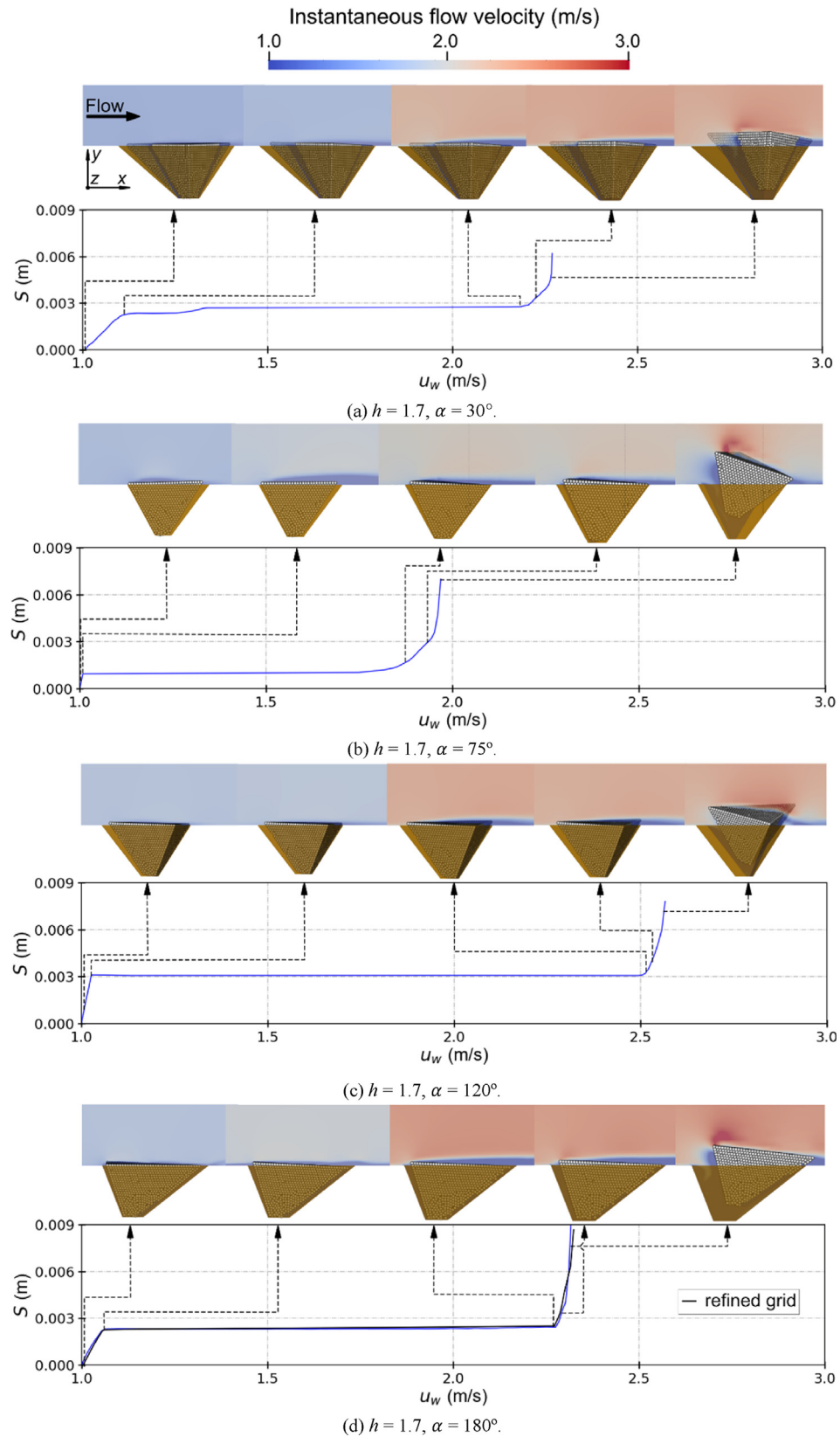


Fig. 5. Streamwise displacement of the modeled blocks. The instantaneous flow velocity field is illustrated at the centerplane of the computational domain. The dotted lines with arrow in each figure indicate the block positions with the increase of u_w .

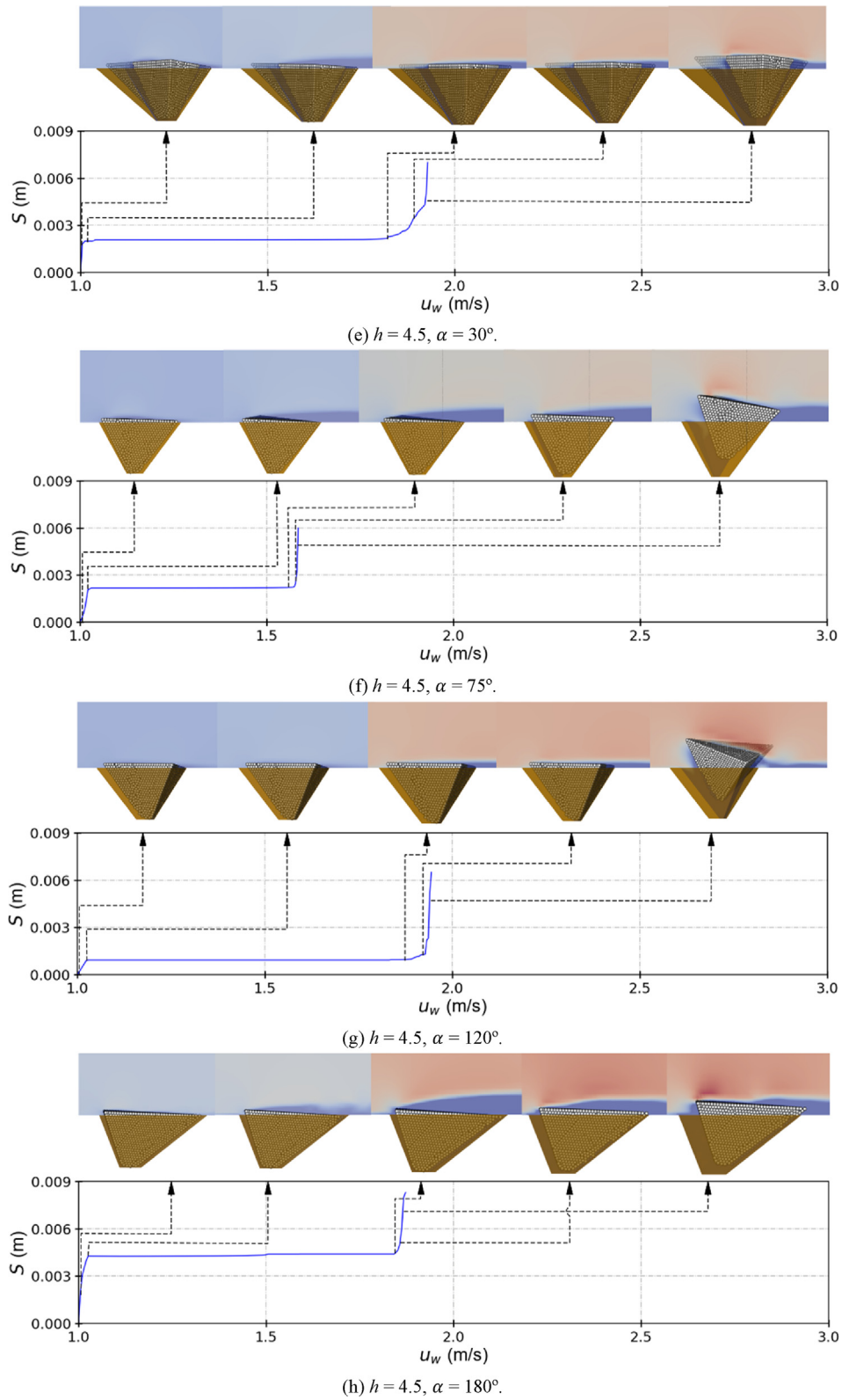


Fig. 5. (continued).

Table 5
Critical flow velocity inducing block incipient motion.

h (mm)	α ($^{\circ}$)	u_{wc} (m/s)
1.7	30	2.19
	75	1.81
	120	2.53
	180	2.3
	180 (refined grid)	2.28
4.5	30	1.82
	75	1.57
	120	1.95
	180	1.84

h since a small change in protrusion can have a significant effect on the uplift of the block. Montgomery (1984) and Reinius (1986) have pointed out that the uplift pressure coefficient for a block could be increased with increasing protrusion height because of the increased local velocity surrounding the exposed block. This is also in line with the results by Lamb et al. (2015), who showed that to

increased protrusion height increase the critical Shields stress and thereby the risk for plucking.

3.2. Trajectory of block movement

Once the incipient motion of a block occurs, the subsequent movement of the block can reflect its failed mode (Tonon, 2007; Lamb et al., 2015). Herein, the block trajectory of each simulation is examined through a combination of observations, monitoring the coordinates of the centroid of the blocks. Fig. 6 presents the trajectory of the motion of the blocks. The blocks appear in translation motion until sliding out of the block mold occurs, and no rotation is observed. Under the value of α , the motion of two different protruding blocks presents a similar tendency. For a fixed h value, the movement behavior of the block is highly dependent on the degree of α . The change of α varies the orientation of the block mold surfaces relative to the streamwise direction, varying the direction of the forces induced by the block mold surfaces. Consequently, the resultant force acting on the block is altered. As a result, the trajectory of the block motion shows different tendencies for different

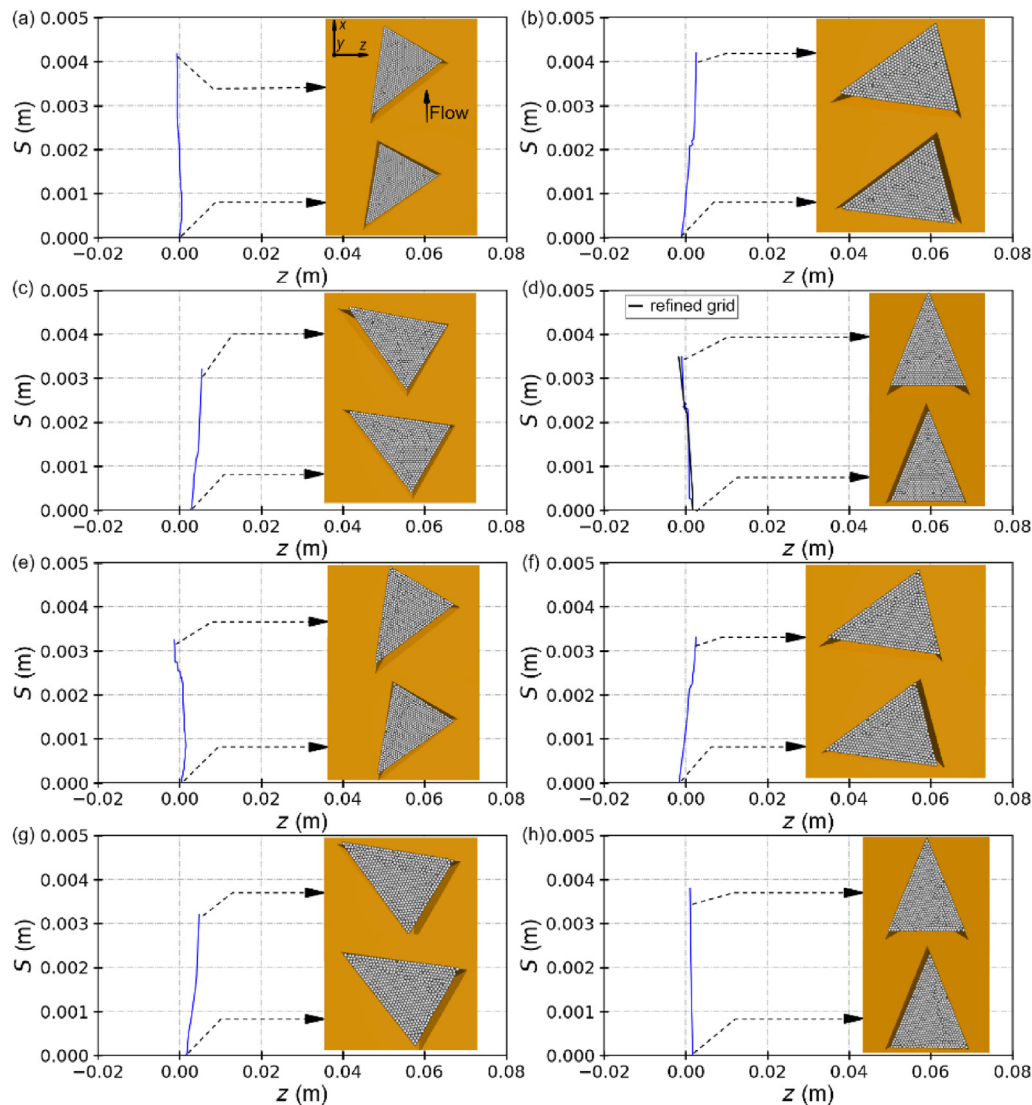


Fig. 6. Trajectory of block motion: (a) $h = 1.7$, $\alpha = 30^{\circ}$; (b) $h = 1.7$, $\alpha = 75^{\circ}$; (c) $h = 1.7$, $\alpha = 120^{\circ}$; (d) $h = 1.7$, $\alpha = 180^{\circ}$; (e) $h = 4.5$, $\alpha = 30^{\circ}$; (f) $h = 4.5$, $\alpha = 75^{\circ}$; (g) $h = 4.5$, $\alpha = 120^{\circ}$; and (h) $h = 4.5$, $\alpha = 180^{\circ}$. The dotted lines with arrow in each figure indicate the block positions.

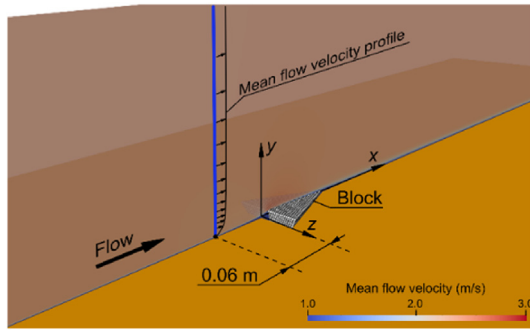


Fig. 7. Mean flow velocity profile of block with $h = 1.7$ mm at $\alpha = 180^\circ$. The mean flow velocity field is at the centerplane of the computational domain.

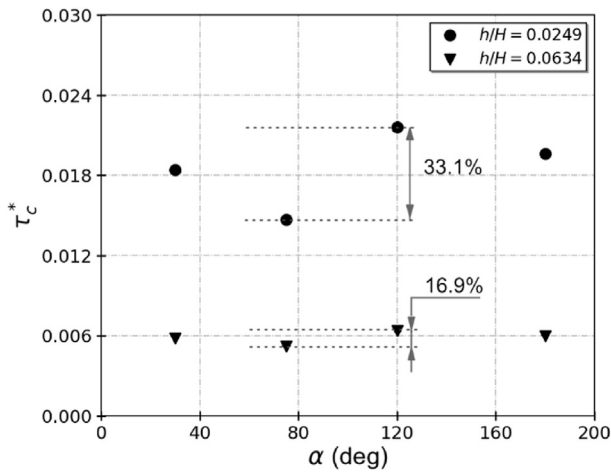


Fig. 8. Critical dimensionless shear stress as a function of block mold orientation.

degrees of α . As $\alpha = 75^\circ$, 120° and 180° , the trajectories of the blocks present a relative constant direction. In contrast, the motion of the blocks at $\alpha = 30^\circ$ shows a varied direction.

As indicated in Figs. 5d and 6d and by the results in Table 5, the refined grid case 5 shows a good agreement with the results obtained in case 4. It implies that the simulation results are independent of the numerical grid.

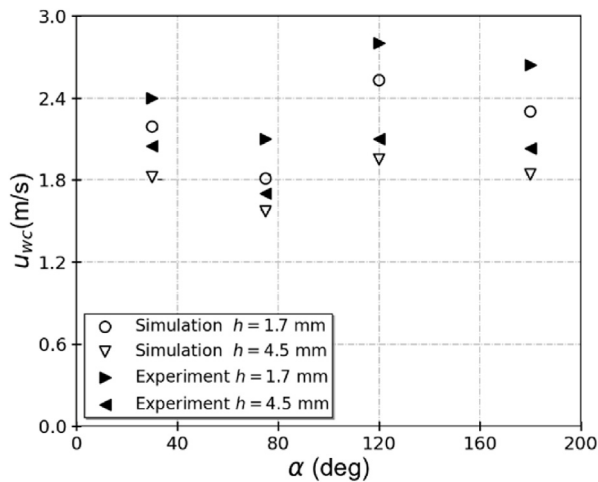


Fig. 9. Comparison with the critical flow velocities over a range of α in the physical experiments.

3.3. Shear stress based description of block incipient motion

For no resistance to motion from surface interactions between the block and block mold, the variables describing the incipient motion of a protruding block are the flow parameters, including critical flow shear velocity (u_{wc}^*), ρ_f , g , μ_f ; and the block parameters of ρ_s , h , and block height (H) (Coleman et al., 2003). Herein, as described in the previous sections, the effect of the block mold surfaces on the blocks' incipient motion is varied as the α changes. Thus, the dimensional analysis yields the following dimensionless parameters describing the blocks' incipient motion in this study:

$$\text{Incipient motion} = f\left(\frac{u_{wc}^*}{gh}, \frac{\rho_s}{\rho_f}, \frac{u_{wc}^*gh}{\mu_f}, \frac{h}{H}, \alpha\right) \quad (14)$$

where the first term is the particle Froude number, the second term is the particle specific gravity, the third term is the particle Reynolds numbers, and the fourth term is the relative protrusion of the block. According to the manner of the analysis of Shields (1936), the first two terms of Eq. (14) can be replaced by the critical dimensionless shear stress, $\tau_c^* = \tau_c/[gh(\rho_s - \rho_f)]$. For fully turbulent flows, the Shields diagram indicates that the threshold of the incipient motion of a particle is not a function of particle Reynolds number formulated as the third term of Eq. (14) (Raudkivi, 1998). Eq. (14) is then reduced to

$$\text{Incipient motion} = f\left(\tau_c^*, \frac{h}{H}, \alpha\right) \quad (15)$$

Herein, the shear stress, τ_c , is derived from the temporally-averaged streamwise velocity profile:

$$\tau_c = \mu \left(\frac{\partial \bar{u}_w}{\partial z} \right) \quad (16)$$

where the flow velocity profile of u_w is obtained at the blue line upstream of block $x = -0.06$ m as shown in Fig. 7.

Fig. 8 presents the τ_c^* as a function of α , with the data grouped according to the relative protrusion height of the block h/H . It is indicated that for a fixed value of α , protrusion has an inherent effect on the erodibility of the block. With an increased value of h/H , the τ_c^* reduces. For a fixed h/H , the value of τ_c^* significantly relies on the degree of α . It is reasonable to hypothesize that the difference of τ_c^* values will narrow down if the value of h/H increases. With the increase of h/H , the largest discrepancy of τ_c^* among degrees of α decreases from 33.1% to 16.9%, which may imply that the effect of block protrusion becomes more dominant on the block incipient motion. As evidenced by the work of Coleman et al. (2003) for protruding fractured rock, the effect of relative protrusion gradually dominates the erodibility of blocks as it becomes larger.

4. Discussions

This study is based on the physical experimental tests conducted by George (2015). He investigated the effects of 3D discontinuity orientation on block erodibility over a range of flow conditions. The results were analyzed to (1) determine the block erodibility threshold and (2) examine the block removal behaviors. As such, the numerical results herein are also analyzed on account of the above aspects and then compared with the experimental data.

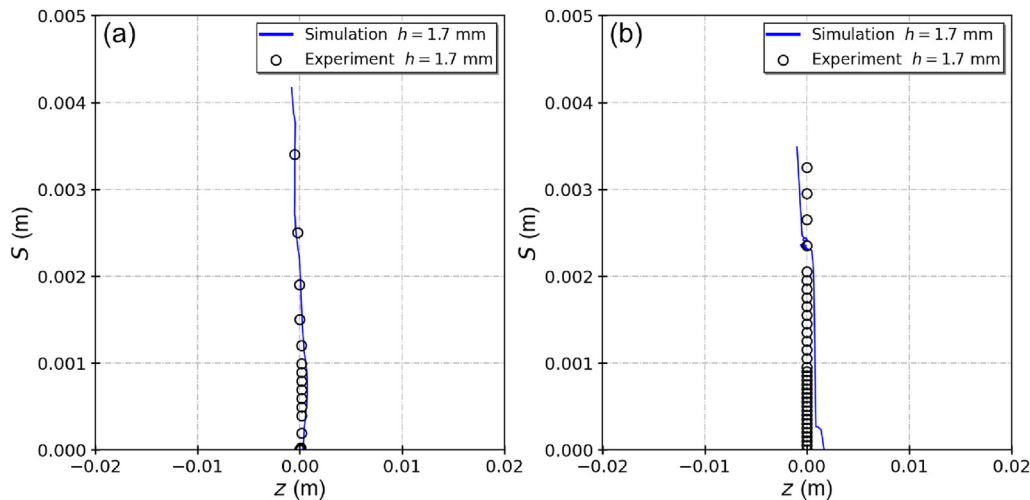


Fig. 10. Comparison with the block trajectories obtained in the physical experiments: (a) $\alpha = 30^\circ$, and (b) $\alpha = 180^\circ$.

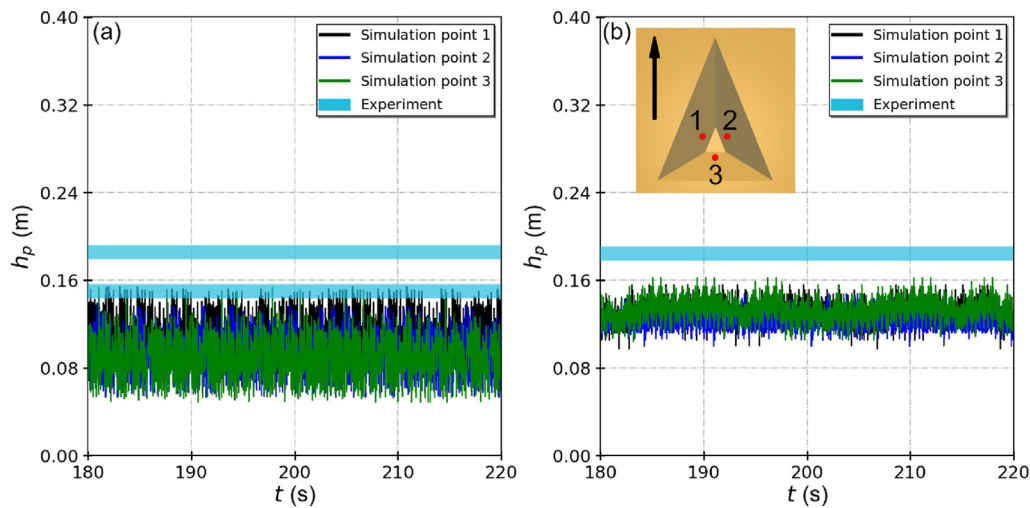


Fig. 11. Comparison with the dynamic flow pressure head obtained in the physical experiments by George (2015): (a) At $\alpha = 30^\circ$, the occurrence of block incipient motion occurred around $t = 190$ s; and (b) At $\alpha = 180^\circ$, the occurrence of block incipient motion occurred around $t = 208$ s.

4.1. Block erodibility threshold

Fig. 9 illustrates the comparison of the numerical results with the experimental data from George (2015). The numerical results present slightly lower critical flow velocities but a similar tendency to the test data. The maximum differences between the numerical results and experimental data are 13.8% and 11.2%, corresponding to $h = 1.7$ mm and 4.5 mm, respectively. These discrepancies may mainly be caused by a combination of protrusion and recession effects of the blocks. Fig. 5 shows the block with a combination of protrusion and recession after the block reaches a temporary steady position, in which the upstream and downstream block edges protrude above and recess below the surface of the channel bed, respectively. As a result, the block protrusion perpendicular to the streamwise direction is increased, lowering the resistance to block incipient motion. This could also be evidenced by the works of Montgomery (1984) and Reinius (1986) that stated that a small increased protrusion could significantly affect block uplift. In addition, the blocks in the numerical simulations are slightly modified compared to the ones in the experiments. Their weights are 8% less than the blocks in the physical experiments. Moreover,

the blocks are reproduced by spherical particles, resulting in a rounded shape of the edges of the blocks rather than a sharp shape as appeared in the experiments. As a result, the flow field around the block edges could be influenced, which may also contribute to the discrepancy.

4.2. Block removal behaviors

George (2015) studied block removal behaviors by analyzing block removal modes and flow characteristics resulting in erosion due to hydraulic loading. The trajectory of block motion reflects the removal modes. Fig. 10 shows the trajectories of numerical results compared with experimental data. Herein only cases 2 and 4 are compared with the data available in George's experiments. The numerical results show a good agreement with the experimental data. At $\alpha = 180^\circ$, the trajectories of the block show a relative constant direction, while a trajectory with a more varied direction is observed at $\alpha = 30^\circ$. This could be explained through the results in Section 3.2, which indicates that the trajectory of the block is mainly dominated by the degree of α . For a fixed α value, the

different blocks could have similar behavior in their movement, as shown in Fig. 6.

In addition, the flow feature leading to the block incipient motion is examined by monitoring the dynamic flow pressure since the dynamic pressure in the fissure may create an uplift pulse inducing the block motion (Hager et al., 2021). In George's experimental tests, the dynamic flow pressure is collected at the surface of the block mold rather than at the surfaces of the block. As such, the dynamic flow pressure head (h_p) of each simulation is obtained at the points as shown in Fig. 11b. Points 1, 2 and 3 are the same as the positions 4, 8 and 12 in the experiment by George (2015). Fig. 11 shows the flow dynamic pressure head during block removal. Like the experimental data, the numerical results show a fairly constant dynamic pressure head from the block incipient motion to block removal. No obvious impulses are monitored at any of the block mold surfaces. This implies that the contribution of dynamic water pressure in the block mold is limited on rock erosion process in the simulation cases, which implies that it is not a critical parameter in this particular case. At $\alpha = 30^\circ$, the experimental data at point 1 show the value in a range of 1.75–1.95 m, and the data at points 2 and 3 are in a range of 1.45–1.55 m. At $\alpha = 180^\circ$, the experimental data at points 1, 2 and 3 are almost the same over a range of 1.72–1.94 m. Compared to the experiments, the value of h_p in the simulations is smaller. The difference comes from the different critical flow velocities between the experiments and simulations. As indicated in Fig. 9, the values of u_{wc} in the simulations are slightly smaller than the values in the experiments, resulting in lower turbulent intensity. As a result, the strength of the dynamic water pressure decreases in the simulations.

4.3. Limitations and further research

This study represents block removal under pure water flow conditions. In practice, the flow inducing rock block erosion usually entrains a large amount of air (Dubinski and Wohl, 2013) and even particles of sediment, which could also affect the rock block erosion process. These aspects could be included in the numerical model by implementing more physics-based models such as two-phase models and are recommended to be studied in future work. Besides, two tetrahedral blocks are used in the simulations rather than rectangular blocks that are closer to real rock blocks. The following work therefore will focus on the erosion process of rectangular blocks. Another limitation of this research is the absence of multi-block influences. Lamb et al. (2015) pointed out that surrounding rock blocks could significantly affect the rock erosion process. In our future work, we will focus on conducting physical and numerical experiments to represent the process of multi-block erosion. Additionally, the fracture aperture is a fixed parameter in this paper. Thus, the influence of fracture aperture on the erosion process is recommended to be studied in future work.

5. Conclusions

This study applied a coupled CFD-DEM approach to simulate the erosion processes of two 3D rock blocks. The two blocks are generated according to the geometries of blocks in physical experimental tests conducted by George (2015). Each block is placed at four different orientations with respect to the streamwise direction. A varied flow condition is then employed to induce the incipient motion of the block. The numerical model describes the interactions between the flowing water and the block, and can reasonably well capture the block removal process. This study, for the first time, attempts to use the coupled FVM-DEM approach to model this interaction behavior that dominates the block erosion

process. Moreover, the removal process of the block is visualized and quantitatively characterized.

Throughout the period of each simulation, the threshold of block incipient motion is determined, which highly rely on the degree of the block's orientation with respect to the streamwise direction. The trajectory of the block movement is subsequently monitored. All blocks appear in translation motion until sliding out of the block mold occurs. Furthermore, the effect of the orientation of the block on the threshold of incipient motion is quantitatively characterized by τ_c^* . The effect of block protrusion gradually plays a dominant role in the block incipient motion as the value of protrusion height increases.

In addition, the simulations yield results in reasonable agreement with the physical experimental data obtained by George. The numerical model is able to capture the block removal behavior since the trajectory of the block observed in the simulations is almost identical to experimental data.

Declaration of competing interest

The authors declare that they have no known competing financial interests or personal relationships that could have appeared to influence the work reported in this paper.

Acknowledgments

The study was carried out as a research project entitled "Numerical modelling of scour in rock spillway channels", funded by the Swedish Hydropower Centre (SVC, www.svc.nu). SVC has been established by the Swedish Energy Agency, Energiforsk AB, and Swedish National Grid (Svenska Kraftnät), together with Luleå University of Technology (LTU), Royal Institute of Technology (KTH), Chalmers University of Technology (CTH), and Uppsala University (UU).

List of symbols

α	Block's orientation with respect to the streamwise direction ($^\circ$)
ϑ	Poisson's ratios of a particle
τ	Fluid stress tensor (Pa)
τ_c	Critical bed shear stress (Pa)
τ_c^*	Dimensionless critical shear stress
δ_n	Overlap distance of two particles (m)
δ_t	Tangential displacement between two particles (m)
ω_p	Angular velocity of a particle (rad/s)
ε_f	Fluid volume fraction in a unit cell
μ_f	Water viscosity (kg/(m s))
ν	Water kinematic viscosity (m^2/s)
ν_t	Sub-grid scale eddy viscosity (m^2/s)
ρ_f	Water density (kg/m^3)
ρ_s	Particle density (kg/m^3)
Δ	Characteristic filter length (m)
∇p	Pressure gradient (N/m^3)
ΔV	Mesh-cell volume (m^3)
C_d	Drag coefficient
C_l	Lift coefficient
C_s	Smagorinsky constant
D	Particle diameter (m)
E	Young's modulus of a particle (Pa)
E^*	Effective Young's modulus (Pa)
e	Coefficient of restitution
$f_{\nabla p}$	Pressure gradient force including buoyancy (N)
f_d	Drag force (N)
f_l	Lift force (N)

f_v	Viscous force (N)
f_n	Normal force between particles (N)
f_s	Tangential force between particles (N)
f_f^p	Averaged interaction force imposed by particles to surrounding fluid in a mesh cell (N)
f_p^c	Contact force between particles (N)
f_p^f	Particle-fluid interaction force acting on a particle by surrounding fluid (N)
f_{pi}^f	Interaction force imposed by the fluid to the i th particle in a cell (N)
f_p^g	Gravitational force of a particle (N)
g	Acceleration of gravity (m/s^2)
G^*	Effective of shear modulus
h	Protrusion height (m)
h_p	Dynamic flow pressure head (m)
H	Block height (m)
I_p	Angular moment of inertia ($kg\ m^2$)
k_n	Elastic stiffness of a particle in the normal direction (N/m)
k_t	Elastic stiffness of a particle in the tangential direction (N/m)
L	Length of block mold (m)
m_p	Mass of a particle (kg)
m_i	Mass of i th particle (kg)
n	Number of a particle
N_p	Particle number inside a cell
R	Particle radius (m)
R^*	Effective of particle radius (m)
Re_r	Relative Reynolds number
r_n	Viscoelastic damping constants of normal contact (kg/s)
r_t	Viscoelastic damping constants of tangential contact (kg/s)
S	Streamwise displacement of the block (m)
S_{ij}	Resolved rate of strain (s^{-1})
T_p^c	Torques due to the contact forces ($kg\ m^2/s^2$)
T_p^f	Torques due to the particle-fluid interaction forces ($kg\ m^2/s^2$)
u_w	Water velocity imposed on the inlet surface of the computational domain (m/s)
u_{wc}	Critical mean water velocity (m/s)
u_{wc}^*	Critical flow shear velocity (m/s)
v_i	Velocity of i th particle (m/s)
V_p	Particle volume (m^3)
\mathbf{v}_f	Velocity of fluid (m/s)
\mathbf{v}_p	Velocity of a particle (m/s)
\mathbf{v}_n	Relative velocity of two particles in a normal direction (m/s)
\mathbf{v}_t	Relative velocity of two particles in a tangential direction (m/s)
x_c	Location of the centroid of the block in the streamwise direction (m)
x_{int}	Initial position of the centroid of the block (m)

References

- Amberger, S., Friedl, M., Goniva, C., Pirker, S., Kloss, C., 2012. Approximation of objects by spheres for multisphere simulations in DEM. In: European Congress on Computational Methods in Applied Sciences and Engineering (ECCOMAS) (Vienna, Austria).
- Annandale, G.W., 1995. Erodibility. *J. Hydraul. Res.* 33 (4), 471–494.
- Annandale, G.W., 2006. *Scour Technology: Mechanics and Engineering Practice*. McGraw-Hill, New York, US.
- Asadollahi, P., Tonon, F., Federspiel, M.P., Schleiss, A.J., 2011. Prediction of rock block stability and scour depth in plunge pools. *J. Hydraul. Res.* 49 (6), 750–756.
- Billstein, M., Hellstadius, K., Johansson, N., Soder, P.E., 2006. Midskog dam in Sweden-Spillway erosion in rock, basis for remedial works. *Transactions of the International Congress on Large Dams* 22 (1), 69.

- Bollaert, E.F., 2002. Transient Water Pressures in Joints and Formation of Rock Scour Due to High-Velocity Jet Impact. PhD Thesis. Laboratory of Hydraulic Constructions, Ecole Polytechnique Federale de Lausanne, Switzerland.
- Bollaert, E.F., Schleiss, A.J., 2005. Physically based model for evaluation of rock scour due to high-velocity jet impact. *J. Hydraul. Eng.* 131 (3), 153–165.
- Chand, R., Khaskheli, M.A., Qadir, A., Ge, B., Shi, Q., 2012. Discrete particle simulation of radial segregation in horizontally rotating drum: effects of drum-length and non-rotating end-plates. *Physica A* 391 (20), 4590–4596.
- Chatanantavet, P., Parker, G., 2009. Physically based modeling of bedrock incision by abrasion, plucking, and macroabrasion. *J. Geophys. Res.: Earth Surf.* 114 (F4).
- Chen, F., Drumm, E.C., Guiochon, G., 2011. Coupled discrete element and finite volume solution of two classical soil mechanics problems. *Comput. Geotech.* 38 (5), 638–647.
- Coleman, S.E., Melville, B.W., Gore, L., 2003. Fluvial entrainment of protruding fractured rock. *J. Hydraul. Eng.* 129 (11), 872–884.
- Dasgupta, B., Basu, D., Das, K., Green, R., 2011. Development of computational methodology to assess erosion damage in dam spillways. In: *Proceedings of the 31st USSD Annual Meeting and Conference* (San Diego, CA, USA).
- Dubinski, I.M., Wohl, E., 2013. Relationships between block quarrying, bed shear stress, and stream power: a physical model of block quarrying of a jointed bedrock channel. *Geomorphology* 180, 66–81.
- Duarte, R.X.M., 2014. Influence of Air Entrainment on Rock Scour Development and Block Stability in Plunge Pools. PhD Thesis. Laboratory of Hydraulic Constructions, Ecole Polytechnique Federale de Lausanne, Switzerland.
- Etmian, V., Lowe, R.J., Ghisalberti, M., 2017. A new model for predicting the drag exerted by vegetation canopies. *Water Resour. Res.* 53 (4), 3179–3196.
- Fantin, D., 2018. CFD-DEM Coupling for Systems of Fluid and Non-spherical Particles. MSc Thesis. Delft University of Technology, Netherlands.
- Federspiel, M.P.E., Bollaert, E.F., Schleiss, A., 2009. Response of an intelligent block to symmetrical core jet impact. In: *Proceedings of the 33rd Congress of IAHR*, pp. 3573–3580. Vancouver, Canada.
- Fiorotto, V., Rinaldo, A., 1992. Fluctuating uplift and lining design in spillway stilling basins. *J. Hydraul. Eng.* 118 (4), 578–596.
- Furuichi, M., Nishiura, D., 2014. Robust coupled fluid-particle simulation scheme in Stokes-flow regime: toward the geodynamic simulation including granular media. *Geochim. Geophys.* 15 (7), 2865–2882.
- Galindo-Torres, S.A., 2013. A coupled Discrete Element Lattice Boltzmann Method for the simulation of fluid–solid interaction with particles of general shapes. *Comput. Methods Appl. Mech. Eng.* 265, 107–119.
- Gardner, M., Sitar, N., 2019. Modeling of dynamic rock–fluid interaction using coupled 3-D discrete element and lattice Boltzmann methods. *Rock Mech. Rock Eng.* 52 (12), 5161–5180.
- Germano, M., Piomelli, U., Moin, P., Cabot, W.H., 1991. A dynamic subgrid-scale eddy viscosity model. *Phys. Fluids A* 3 (7), 1760–1765.
- George, M.F., Sitar, N., 2012. Block Theory Application to Scour Assessment of Unlined Rock Spillways. Technical Report No. UCB GT, 12–02. University of California.
- George, M.F., 2015. PhD Thesis 3D Block Erodibility: Dynamics of Rock-Water Interaction in Rock Scour. UC Berkeley, (California, USA).
- George, M.F., Sitar, N., 2016. System reliability approach for rock scour. *Int. J. Rock Mech. Min.* 85, 102–111.
- Goniva, C., Kloss, C., Deen, N.G., Kuipers, J.A., Pirker, S., 2012. Influence of rolling friction on single spout fluidized bed simulation. *Particuology* 10 (5), 582–591.
- Guo, Y., Wassgren, C., Ketterhagen, W., Hancock, B., James, B., Curtis, J., 2012. A numerical study of granular shear flows of rod-like particles using the discrete element method. *J. Fluid Mech.* 713, 1–26.
- Hager, W.H., Schleiss, A.J., Boes, R., Pfister, M., 2021. Chapter 6.5 rock scour. In: *Hydraulic Engineering of Dams*. CRC Press.
- Han, Y., Cundall, P.A., 2011. Resolution sensitivity of momentum-exchange and immersed boundary methods for solid–fluid interaction in the lattice Boltzmann method. *Int. J. Numer. Methods Fluids* 67 (3), 314–327.
- Kloss, C., Goniva, C., Hager, A., Amberger, S., Pirker, S., 2012. Models, algorithms and validation for opensource DEM and CFD–DEM. *Prog. Comput. Fluid Dyn.* 12 (2–3), 140–152.
- Khosronejad, A., Kang, S., Borazjani, I., Sotiropoulos, F., 2011. Curvilinear immersed boundary method for simulating coupled flow and bed morphodynamic interactions due to sediment transport phenomena. *Adv. Water Resour.* 34 (7), 829–843.
- Khosronejad, A., Hill, C., Kang, S., Sotiropoulos, F., 2013. Computational and experimental investigation of scour past laboratory models of stream restoration rock structures. *Adv. Water Resour.* 54, 191–207.
- Koulibaly, A.S., Saedi, A., Rouleau, A., Quirion, M., 2022. A reduced-scale physical model of a spillway to evaluate the hydraulic erodibility of a fractured rock mass. *Rock Mech. Rock Eng.* 56, 933–951.
- Kruggel-Emden, H., Rickelt, S., Wirtz, S., Scherer, V., 2008. A study on the validity of the multi-sphere discrete element method. *Powder Technol.* 188 (2), 153–165.
- Lamb, M.P., Finnegan, N.J., Scheingross, J.S., Sklar, L.S., 2015. New insights into the mechanics of fluvial bedrock erosion through flume experiments and theory. *Geomorphology* 244, 33–55.
- Lysenko, D.A., Ertesvåg, I.S., Rian, K.E., 2012. Large-eddy simulation of the flow over a circular cylinder at Reynolds number 3900 using the OpenFOAM toolbox. *Flow, Turbul. Combust* 89 (4), 491–518.

- Lysenko, D.A., Ertesvåg, I.S., Rian, K.E., 2014. Large-eddy simulation of the flow over a circular cylinder at Reynolds number 2×10^4 . *Flow, Turbul. Combust* 92 (3), 673–698.
- Lloyd, T.P., James, M., 2015. Large eddy simulations of a circular cylinder at Reynolds numbers surrounding the drag crisis. *Appl. Ocean Res.* 59, 676–686.
- Li, A., Liu, P., 2010. Mechanism of rock-bed scour due to impinging jet. *J. Hydraul. Res.* 48 (1), 14–22.
- Melo, J.F., Pinheiro, A.N., Ramos, C.M., 2006. Forces on plunge pool slabs: influence of joints location and width. *J. Hydraul. Eng.* 132 (1), 49–60.
- Melville, B., Van Ballegooy, R., Van Ballegooy, S., 2006. Flow-induced failure of cable-tied blocks. *J. Hydraul. Eng.* 132 (3), 324–327.
- Mindlin, R.D., Deresiewicz, H., 1952. Elastic spheres in contact under varying oblique forces. *J. Applied Mech.* 20 (3), 327–344.
- Montgomery, R.A., 1984. Investigation into rock erosion by high velocity water flows. In: *Bull. No. TRITA-VBI-128*. Royal Institute of Technology (Stockholm, Sweden).
- Nan, X., Hou, J., Shen, Z., et al., 2022. CFD-DEM coupling with multi-sphere particles and application in predicting dynamic behaviors of drifting boats. *Ocean Eng* 247, 110368.
- Owen, D.R.J., Leonardi, C.R., Feng, Y.T., 2011. An efficient framework for fluid–structure interaction using the lattice Boltzmann method and immersed moving boundaries. *Int. J. Numer. Methods Eng.* 87 (1–5), 66–95.
- Pells, S.E., Pells, P.J., Peirson, W.L., Douglas, K., Fell, R., 2015. Erosion of unlined spillways in rock—does a “scour threshold” exist? *ANCOLD*. In: *Contemporary Challenges for Dams*. Proceedings of the Annual Australian National Committee on Large Dams Conference, vol. 4, 8.
- Raudkivi, A.J., 1998. *Loose Boundary Hydraulics*. A.A. Balkema, Rotterdam, the Netherlands.
- Reinius, E., 1986. Rock erosion. *Int. Water Power Dam Constr.* 38 (6), 43–48.
- Rettinger, C., Rüde, U., 2022. An efficient four-way coupled lattice Boltzmann–discrete element method for fully resolved simulations of particle-laden flows. *J. Comput. Phys.* 453, 110942.
- Robinson, M., Ramaioli, M., Luding, S., 2014. Fluid–particle flow simulations using two-way-coupled mesoscale SPH–DEM and validation. *Int. J. Multiph. Flow* 59, 121–134.
- Schmeeckle, M.W., 2014. Numerical simulation of turbulence and sediment transport of medium sand. *J. Geophys. Res.: Earth Surf.* 119 (6), 1240–1262.
- Soundararajan, K.K., 2015. *Multi-scale multiphase modelling of granular flows*. In: *PhD Thesis*. University of Cambridge (Cambridge, England).
- Sun, R., Xiao, H., 2016a. CFD–DEM simulations of current-induced dune formation and morphological evolution. *Adv. Water Resour.* 92, 228–239.
- Saffman, P.G., 1968. The lift on a small sphere in a slow shear flow- Corrigendum. *J. Fluid Mech.* 31 (3), 624.
- Shields, A., 1936. *Application of Similarity Principles and Turbulence Research to Bed-Load Movement*. Hydrodynamics Laboratory, California Institute of Technology, Pasadena, USA. Publication No. 167 (English translation).
- Shen, Z., Wang, G., Huang, D., Jin, F., 2022. A resolved CFD-DEM coupling model for modeling two-phase fluids interaction with irregularly shaped particles. *J. Comput. Phys.* 448, 110695.
- Sun, R., Xiao, H., 2016b. SediFoam: a general-purpose, open-source CFD–DEM solver for particle-laden flow with emphasis on sediment transport. *Comput. Geosci.* 89, 207–219.
- Sun, R., Xiao, H., Sun, H., 2017. Realistic representation of grain shapes in CFD–DEM simulations of sediment transport with a bonded-sphere approach. *Adv. Water Resour.* 107, 421–438.
- Teng, P., Zhang, S., Johansson, F., 2021. Numerical modelling of incipient motion of fracture infillings. *Int. J. Rock Mech. Min. Sci.* 148, 104960.
- Tonon, F., 2007. Analysis of single rock blocks for general failure modes under conservative and non-conservative forces. *Int. J. Numer. Anal. Methods Geomech.* 31 (14), 1567–1608.
- Tsuji, Y., Kawaguchi, T., Tanaka, T., 1993. Discrete particle simulation of two-dimensional fluidized bed. *Powder Technol.* 77 (1), 79–87.
- Wang, D., 2019. *Direct Numerical Simulation of Coupled Fluid-Particle Flow in Hydraulic Fractures*. PhD Thesis. University of Queensland, Queensland, Australia.
- Whipple, K.X., Snyder, N.P., Dollenmayer, K., 2000a. Rates and processes of bedrock incision by the upper Ukak river since the 1912 Novarupta ash flow in the valley of ten Thousand Smokes, Alaska. *Geology* 28, 835–838.
- Whipple, K.X., Hancock, G.S., Anderson, R.S., 2000b. River incision into bedrock: mechanics and relative efficiency of plucking, abrasion, and cavitation. *Geol. Soc. Am. Bull.* 112, 490–503.
- Wohl, E.E., 1993. Bedrock channel incision along Piccaninny Creek, Australia. *J. Geol.* 101, 749–761.
- Zhao, J., Shan, T., 2013. Coupled CFD–DEM simulation of fluid–particle interaction in geomechanics. *Powder Technol.* 239, 248–258.
- Zhao, T., Houlisby, G.T., Utili, S., 2014. Investigation of granular batch sedimentation via DEM–CFD coupling. *Granul. Matter* 16 (6), 921–932.
- Zhang, H., Tan, Y., Shu, S., et al., 2014. Numerical investigation on the role of discrete element method in combined LBM–IBM–DEM modeling. *Comput. Fluids* 94, 37–48.
- Zhou, Z.Y., Kuang, S.B., Chu, K.W., Yu, A.B., 2010. Discrete particle simulation of particle–fluid flow: model formulations and their applicability. *J. Fluid Mech.* 661, 482–510.



Penghua Teng completed his BSc degree in Industrial Design at Chang'an University, China, in 2010. Subsequently, he obtained his MSc degree in Fluid Mechanics from Northwestern Polytechnical University, China, in 2013. He attained his Licentiate and PhD in Hydraulic and Hydrologic Engineering from the KTH-Royal Institute of Technology, Sweden, in 2017 and 2019, respectively. He served as a Researcher in the Division of Rock Mechanics at KTH-Royal Institute of Technology from 2019 to 2021. Currently, he is affiliated with the Division of Fluid and Experimental Mechanics at the Luleå University of Technology (LTU) in Sweden. His research interests include (1) physical hydraulic modelling and general hydraulic investigations, focusing on issues such as spillway energy dissipation, dam-break problems, high-velocity two-phase flow modelling, hydraulic transients in hydropower plants, and seepage flows in embankment dams; and (2) the theoretical study and numerical modelling of water–solid coupling processes, including rock erosion in spillway channels, and internal erosion of fracture infilling materials in dam foundations. He has been participated in the projects from Svenskt vattenkraftcentrum (Swedish Hydropower Centre).